

Copy-Move Image Forgery Detection Based on Evolving Circular Domains Coverage

Shilin Lu, Xinghong Hu, Chengyou Wang, Lu Chen, Shulu Han, Yuejia Han,

Abstract—The aim of this paper is to improve the accuracy of copy-move forgery detection (CMFD) in image forensics by proposing a novel scheme and the main contribution is evolving circular domains coverage (ECDC) algorithm. The proposed scheme integrates both block-based and keypoint-based forgery detection methods. Firstly, speed-up robust feature (SURF) in log-polar space and scale invariant feature transform (SIFT) are extracted from an entire image. Secondly, generalized 2 nearest neighbor (g2NN) is employed to get massive matched pairs. Then, random sample consensus (RANSAC) algorithm is employed to filter out mismatched pairs, thus allowing rough localization of counterfeit areas. To present these forgery areas more accurately, we propose the efficient and accurate ECDC algorithm to present them. This algorithm can find satisfactory threshold areas by extracting block features from jointly evolving circular domains, which are centered on matched pairs. Finally, morphological operation is applied to refine the detected forgery areas. The experimental results indicate that the proposed CMFD scheme can achieve better detection performance under various attacks compared with other state-of-the-art CMFD schemes.

Index Terms—Image forensics, copy-move forgery detection (CMFD), scale invariant feature transform (SIFT), speed-up robust feature (SURF), evolving circular domains coverage (ECDC).

1 INTRODUCTION

WITH the development of computer and image processing software, digital image tampering becomes much easier; therefore, lots of digital images lack authenticity and integrity, which poses a threat to many critical fields. For example, it may lead to misdiagnosis when forged images are used in medical fields [1], and forged newspaper photographs may mislead people and cause unnecessary social unrest [2]. Hence, the ability to credibly authenticate an image has become a major focus of image forensics and security.

The existing detection techniques fall into two main categories: active and passive. Active forensics techniques ensure the authenticity of digital images by verifying the integrity of authentication information, such as digital watermark [3]–[5] and digital signature [6]–[8]. These active methods have strong detection abilities and cannot be easily avoided, but their main defect is that the watermark must be inserted as a key into the image. Passive forensics techniques are used to verify the authenticity by analyzing the information and structure of the image, which overcomes the disadvantage of active forensics techniques.

This work was supported in part by the Shandong Provincial Natural Science Foundation, China (Nos. ZR2021MF060, ZR2017MF020), in part by the Education and Teaching Reform Research Project of Shandong University, Weihai (No. Y2021054), in part by the National Natural Science Foundation of China (No. 61702303), in part by the Science and Technology Development Plan Project of Weihai Municipality in 2020, and in part by the 14th Student Research Training Program (SRTP) at Shandong University, Weihai (No. A19167).

Chengyou Wang
 School of Mechanical, Electrical and Information Engineering, Shandong University, Weihai 264209, China
 Tel.: +86-631-5688338
 e-mail: wangchengyou@sdu.edu.cn

There are two main forgeries that alter the contents of images: splicing and copy-move. The common splicing forgery method consists in copying and pasting a part of an image into another image, while the copy-move forgery method is a way to copy and paste a part of an image into the same image. In recent years, copy-move forgery has become one of the most popular subtopics in forgery detection [9]. To make copy-move tampered images more trustworthy, some processing methods are probably required, including in particular: rotation, scaling, downsampling, JPEG compression, and noise addition. Considering that image copy-move forgery detection (CMFD) is a challenging topic, this paper focuses on CMFD algorithms.

The general steps of CMFD are feature extraction, feature matching, and postprocessing. Based on different extracting features, CMFD is divided into block-based, keypoint-based, and fusion of these two methods. The last one has become more popular in recent years.

In this paper, we propose a CMFD scheme based on evolving circular domains coverage (ECDC), which combines block-based and keypoint-based methods. It extracts two different descriptors from an image, and then we match and filter those descriptors to obtain a rough localization. After that, we employ the proposed ECDC algorithm to cover forgery areas. The refined forgery areas are obtained by postprocessing ultimately. The two main contributions of this paper are listed below:

1) Our first contribution is that we combine speed-up robust feature (SURF) in log-polar space and scale invariant feature transform (SIFT) as descriptors to depict a host image more accurately. This cannot only raise the precision of the proposed scheme under plain copy-move forgery evidently, but also improve its robustness to various geometric transformations and signal processing.

2) Our second contribution is that we propose a novel algorithm, named ECDC, to present forgery areas exactly. By comparing the differences of block features in jointly evolving circular domains, this algorithm which is based on the pre-positioning of keypoints can greatly reduce computational complexity and improve its running efficiency. In addition, ECDC cannot only cover large-scale tampered areas completely, but also depict small areas accurately.

The rest of this paper is organized as following: Section II briefly reviews the related work of CMFD; Section III displays the framework of the proposed CMFD scheme and then explains each step in details; Section IV shows the experimental results of CMFD and their analysis; finally, Section V contains the conclusion.

2 RELATED WORK

In this section, we review some classic and state-of-the-art CMFD schemes. Based on the difference of extracted features from the image, we divide this review into the following parts: block-based method, keypoint-based method, and fusion of the two methods.

2.1 Block-Based Methods

The block-based CMFD methods, in general, divide a host image into small, regular, and overlapped blocks. After extracting features of each subblock, the results are obtained by matching and postprocessing those features. Fridrich *et al.* [10] proposed the CMFD algorithm, which is a milestone in the field of CMFD. They used quantified discrete cosine transform (DCT) coefficients as features. Then, a lexicographically ordered feature matrix reducing the range of feature matching, was used to detect similar regions [9]. Popescu and Farid [11] used principal components analysis (PCA) as features to detect tampered areas. Bayram *et al.* [12] proposed Fourier-Mellin transform (FMT) to extract features. They applied counting bloom filters instead of Lexicographic sorting as a matching scheme which was more efficient. Wang *et al.* [13], [14] used the Gaussian pyramid to reduce the dimensions of images. The former used the Hu-moments of blocks, and the latter employed the mean value of image pixels in circle blocks, which were divided into concentric circles. Ryu *et al.* [15] proposed a method based on rotationally-invariant Zernike moments, which can detect forged regions even though they are rotated. Li [16] proposed an algorithm that matched polar cosine transform (PCT) with locality sensitive hashing (LSH), which required simpler calculations than Zernike moments. This algorithm excels at large-scale rotation. Similarly, polar sine transform (PST) and polar complex exponential transform (PCET) also belong to polar harmonic transform (PHT) [17]. Cozzolino *et al.* [18], [19] proposed a new matching method called PatchMatch, and a fast postprocessing procedure based on dense linear fitting. This method greatly reduces the computational complexity and it is robust to various types of distortions.

Overall, although applying Lexicographic sorting and reducing dimensions make block-based methods detection more efficient, it still has higher computational complexity than keypoint-based methods. In addition, when faced with

large-scale scaling, the robustness of block-based methods, in general, is significantly reduced.

2.2 Keypoint-Based Methods

The keypoint-based CMFD methods usually extract features from an entire image, which is the main difference from block-based methods, and they effectively reduce computational complexity. Huang *et al.* [20] proposed the best-bin-first nearest neighbor identification algorithm based on SIFT. Xu *et al.* [21] proposed SURF to extract features with a faster speed compared with SIFT. Amerini *et al.* [22] used generalized 2 nearest neighbor (g2NN) on SIFT descriptor to obtain qualified features. Then the random sample consensus (RANSAC) was used to remove mismatched points. Shivakumar and Baboo [23] proposed a CMFD scheme based on SURF and kd-tree for multidimensional data matching. In high-resolution image processing process, this method can detect different sizes of copied regions with a minimum number of false matches. To present tampered areas accurately, Pan and Lyu [24] proposed using RANSAC to estimate the affine transformation matrix, and then they obtained correlation maps by calculating correlation coefficients to locate forged regions.

However, references [22], [23] only roughly marked the detected regions with connections on matched pairs. Furthermore, when tampering occurs in low-entropy or small-size areas, the detection results are unsatisfying due to the small number of keypoints.

2.3 Fusion of Block-Based and Keypoint-Based Methods

For better detection performance, combining the advantages of block-based and keypoint-based methods have currently become a trend. Pun *et al.* [25] used adaptive over-segmentation algorithm to divide the host image into non-overlapping and irregular blocks. They also proposed a new forgery region extraction algorithm by replacing feature points with small superpixels to generate detected regions. But the accuracy of the localization depends on the initial size of superpixels and the detected results have fuzzy boundaries. Zheng *et al.* [26] classified the host image into textured and smooth regions in which, SIFT and Zernike features were respectively extracted and matched. However, this method cannot accurately distinguish between smooth and textured areas, especially when tampered regions are attacked by noise. Zandi *et al.* [27] proposed a new interest point detector and used an effective filtering algorithm and an iteration algorithm to improve their performance. Although they can effectively detect tampered areas in low contrast areas, their detected results usually contain mismatches. Pun and Chung [28] proposed a two-stage localization for CMFD. The weber local descriptor (WLD) was extracted from each superpixel in their rough localization stage, and in their precise localization stage, discrete analytic Fourier-Mellin transform (DAFMT) of roughly located areas were extracted. Wang *et al.* [29] classified irregular and non-overlapping image blocks into smooth and textured regions. They combined RANSAC algorithm with a filtering strategy to eliminate false matches. This method can detect a high-brightness smooth forgery. However, these two methods

[28], [29] achieve high detecting accuracy at the expense of running efficiency.

In summary, the main problems faced by block-based CMFD methods are the inability to detect images with large-scale scaling and high computational complexity, while the main problem of keypoint-based CMFD methods is that there are fewer keypoints in low-entropy areas, which lead to incomplete coverage of tampered areas. Fusing block-based and keypoint-based methods reasonably can preserve their advantages and avoid certain shortcomings at the same time. Our scheme fairly integrates block-based and keypoint-based methods, which results in complete coverage of tampered areas and higher detection efficiency. The algorithm is described in more detail in Section III.

3 PROPOSED COPY-MOVE FORGERY DETECTION SCHEME

In this section, we explicate our CMFD scheme. The framework of the whole scheme is given in Fig. 1. Firstly, we extract both SIFT descriptor and log-polar SURF descriptor (LPSD) from an entire image. Secondly, g2NN is employed on each descriptor to obtain massive matched pairs. Then, we employ RANSAC to eliminate mismatched pairs. Finally, the ECDC algorithm is used to present entire forgery regions through those matched pairs. In the rest of this section, Section III-A explains the feature extraction algorithm combining SIFT and LPSD; Section III-B introduces the keypoints matching algorithm using g2NN; Section III-C describes the process of eliminating mismatched pairs by using RANSAC; Section III-D explains in detail how matched pairs are expanded to whole forgery regions by using ECDC algorithm.

3.1 Feature Extraction Using Combination of SIFT and LPSD

In this section, we explain how to extract keypoints as descriptors of the image. SIFT and SURF algorithms have been widely used in the field of computer vision in recent years. These keypoints are robust to various attacks, including rotation, scaling, downsampling, JPEG compression, and noise addition. As a result, SIFT and SURF are often used to extract keypoints in existing keypoint-based methods. In this paper, unlike in general keypoint-based methods, we combine SIFT and LPSD to depict images.

3.1.1 SIFT

Lowe [30] decomposed the SIFT algorithm into the following four steps: firstly, extrema in scale space were located with the computation searching over all scales and image locations; secondly, at each candidate location, keypoints were selected based on measures of their stability; then, based on local image gradient directions, one or more orientations were assigned to each keypoint location; at last, the local image gradients were measured at the selected scale in the region around keypoint to generate descriptors.

In general, the extreme points of a given image are detected at different scales in scale space, which is constructed by using the Gaussian pyramids with different Gaussian smoothing and resolution subsampling. These keypoints are

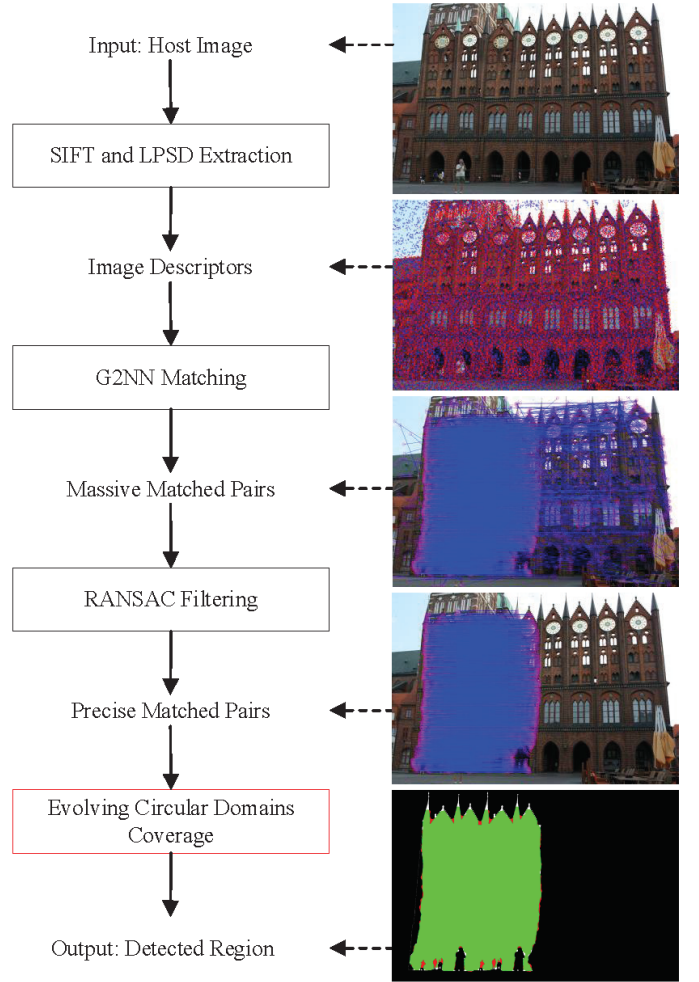


Figure 1. Framework of the proposed copy-move forgery detection scheme. In the second image, SIFT is labeled with blue circles and LPSD is labeled with red dots.

extracted by applying difference of Gaussian (DoG), and a DoG image D is denoted by [30]:

$$D(x, y, \sigma) = [G(x, y, k\sigma) - G(x, y, \sigma)] * I(x, y) \quad (1) \\ = L(x, y, k\sigma) - L(x, y, \sigma),$$

where $L(x, y, k\sigma)$ is the convolution of the original image $I(x, y)$, with the Gaussian blur $G(x, y, \sigma)$ at scale space k .

To ensure rotation invariance, for each keypoint, the algorithm assigns a canonical orientation which can be determined by calculating the gradient in its neighborhood. Specifically, for an image sample $L(x, y, \sigma)$ at scale σ , the gradient magnitude $m(x, y)$ and orientation $\theta(x, y)$ can be pre-calculated using pixel difference as follows [30]:

$$m(x, y) = [[L(x + 1, y) - L(x - 1, y)]^2 \\ + [L(x, y + 1) - L(x, y - 1)]^2]^{\frac{1}{2}}, \quad (2)$$

$$\theta(x, y) = \tan^{-1} \frac{L(x, y + 1) - L(x, y - 1)}{L(x + 1, y) - L(x - 1, y)}. \quad (3)$$

3.1.2 SURF

SURF proposed by Bay *et al.* [31] is an improvement on SIFT, and being faster is its prominent characteristic. By

using a Hessian matrix for optimization, SURF algorithm accelerates SIFT detection process without reducing the quality of the detected points. Then, different size box filters are used to establish scale space and to convolute with the integral image. Given a point $\mathbf{x} = (x, y)$ in an image I , the Hessian matrix $\mathbf{H}(\mathbf{x}, \sigma)$ in \mathbf{x} at scale σ is represented as follows [31]:

$$\mathbf{H}(\mathbf{x}, \sigma) = \begin{bmatrix} L_{xx}(\mathbf{x}, \sigma) & L_{xy}(\mathbf{x}, \sigma) \\ L_{xy}(\mathbf{x}, \sigma) & L_{yy}(\mathbf{x}, \sigma) \end{bmatrix}, \quad (4)$$

where $L_{xx}(\mathbf{x}, \sigma)$ is the convolution result of the second order derivative of Gaussian filter with the image I in point \mathbf{x} , and similarly for $L_{xy}(\mathbf{x}, \sigma)$ and $L_{yy}(\mathbf{x}, \sigma)$.

Hessian matrix and non-maximum suppression are used to detect potential keypoints. While assigning one or more canonical orientations, the dominant orientation of the Gaussian weighted Harr wavelet responses can be detected by a sliding orientation window at every sample point within a circular neighborhood around the interest point.

3.1.3 Combination of SIFT and LPSD

Kaura and Dhavale [32] showed that the combination of SIFT and SURF would improve the detection performance of the keypoint-based method. In consideration of the lower detection accuracy of SURF, compared with SIFT [33], we improve this accuracy by applying log-polar coordinates to it [34]. It can be seen in experiments that SURF in log-polar space, whose detection results are much more accurate than SIFT, succeeds well in detecting plain copy-move forgery, especially for detailed objects. Fig. 2(a1)–(a3) and Fig. 2(b1)–(b3) show, respectively, SIFT and LPSD matched results for plain copy-move forgery (the matching algorithm is explained in Section III-B). We can observe that LPSD can obtain more matched pairs on small or detailed areas from Fig. 2(a3) and (b3). However, SIFT exhibits a surprising stability when forgery regions are attacked by noise or any other manipulations, as shown in Fig. 2(a4) and (b4). In these two figures, noise with standard deviation of 0.1 has been added to the copied fragments; thus, we easily find that LPSD hardly detect any right matched pairs while SIFT performs well. Thus, we decide to combine SIFT and LPSD to make up the instability of LPSD while forgery regions are attacked.

3.2 Multiple Keypoints Matching

3.2.1 g2NN

After feature extraction, two descriptor groups are obtained:

$$\mathbf{f}^{\text{SIFT}} = \{f_1^{\text{SIFT}}, f_2^{\text{SIFT}}, \dots, f_n^{\text{SIFT}}\}, \quad (5)$$

$$\mathbf{f}^{\text{LPSD}} = \{f_1^{\text{LPSD}}, f_2^{\text{LPSD}}, \dots, f_m^{\text{LPSD}}\}, \quad (6)$$

where \mathbf{f}^{SIFT} is the n dimensional SIFT descriptor vector and \mathbf{f}^{LPSD} is the m dimensional LPSD descriptor vector. To find similar descriptors in the image, we need to match them to each other. Lowe [35] employed the distance ratio between the nearest neighbor and the second-nearest neighbor to compare it with a threshold T . Only if the ratio is less than T , the keypoints are matched. However, this matching process is unable to manage multiple keypoints matching. Since the same image areas may be cloned over and over in

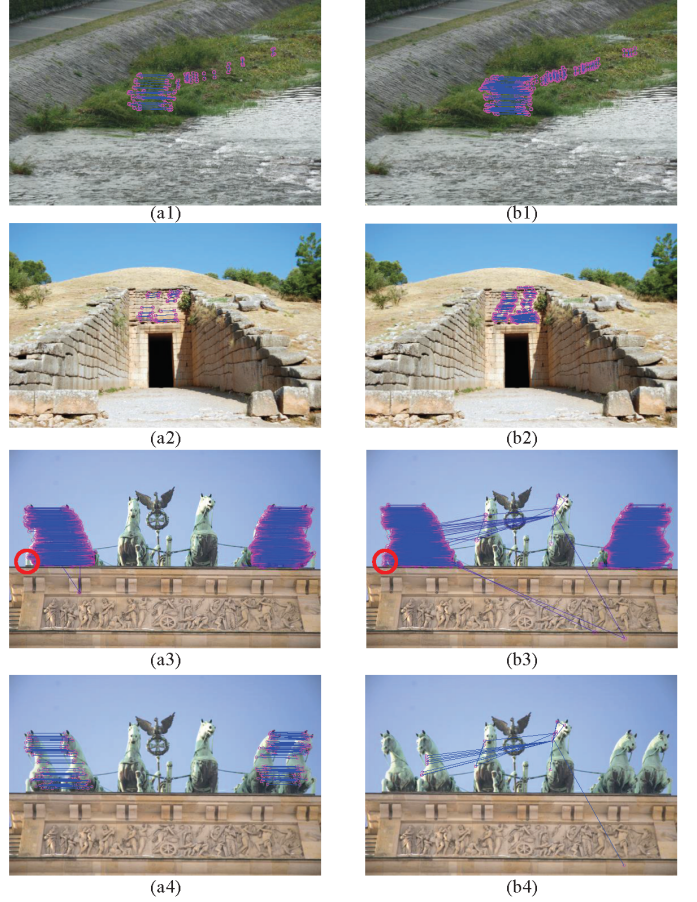


Figure 2. Comparison of SIFT (left) and LPSD (right) detection results. First three rows: SIFT and LPSD detection results under plain copy-move forgery; fourth row: SIFT and LPSD detection results under local noise attack where the standard deviation is 0.1.

a tampered image, we employ g2NN algorithm [22] which can cope with multiple copies of the same descriptors. Specifically, taking SIFT as an example, we define a sorted distance vector χ_i for $\mathbf{f}_i^{\text{SIFT}}$ to represent the Euclidean distance between $\mathbf{f}_i^{\text{SIFT}}$ and the other $(n-1)$ descriptors, i.e.,

$$\chi_i = \{d_{i,1}, d_{i,2}, \dots, d_{i,n}\}, \quad (7)$$

where $d_{i,j} (i, j = 1, 2, \dots, n; i \neq j)$ is the Euclidean distance between $\mathbf{f}_i^{\text{SIFT}}$ and $\mathbf{f}_j^{\text{SIFT}}$, i.e.,

$$d_{i,j} = \left\| \mathbf{f}_i^{\text{SIFT}} - \mathbf{f}_j^{\text{SIFT}} \right\|_2. \quad (8)$$

To facilitate the finding of an appropriate threshold, we measure the similarity between descriptors by using $d_{i,j}^2$ (the Euclidean distance square). Thus, for all \mathbf{f}^{SIFT} , an $n \times (n-1)$ matrix ξ will be generated:

$$\xi = \begin{bmatrix} \chi_1^2 \\ \chi_2^2 \\ \vdots \\ \chi_n^2 \end{bmatrix} = \begin{bmatrix} d_{1,2}^2 & d_{1,3}^2 & \cdots & d_{1,n}^2 \\ d_{2,1}^2 & d_{2,3}^2 & \cdots & d_{2,n}^2 \\ \vdots & \vdots & & \vdots \\ d_{n,1}^2 & d_{n,2}^2 & \cdots & d_{n,n-1}^2 \end{bmatrix}. \quad (9)$$

We iterate 2 nearest neighbor (2NN) algorithm on every row of the distance matrix ξ to find multiple copies. Based on χ_i as an example, the iteration will stop when

$$d_{i,j}^2 / d_{i,j+1}^2 > T. \quad (10)$$

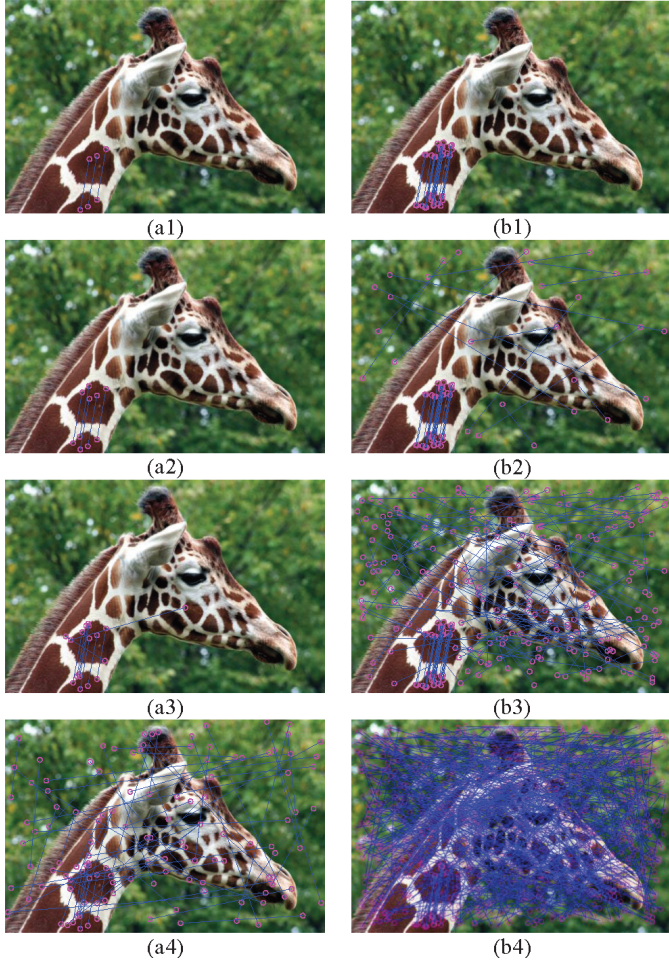


Figure 3. Comparison of matches under different g2NN thresholds for SIFT (left) and LPSD (right) descriptors.

If the iteration stops at $d_{i,k}^2$, each keypoint corresponding to the distance in $\{d_{i,1}^2, d_{i,2}^2, \dots, d_{i,k}^2\}$ (where $k = 1, 2, \dots, n; k \neq i$) is considered as a match for the inspected keypoint.

3.2.2 Threshold T

Huang *et al.* [20] analyzed that, if the ratio T of the distance is reduced, the number of matched keypoints will be reduced, but the matching accuracy will be improved. In order to test and verify this conclusion, we set different thresholds and observe the number of matched pairs and mismatched pairs of f^{SIFT} and f^{LPSD} under plain copy-move forgery. We use Figs. 3 and 4 to perceptibly and statistically describe the result. Fig. 3(a1)–(a4) and Fig. 3(b1)–(b4) show separately detected results of SIFT and LPSD, where thresholds range from 0.1 to 0.7 in steps of 0.2. To select an appropriate threshold, we randomly selected 100 images, including plain copy-move, rotation, scaling, noise, and other attacks, from the benchmark dataset [9] for g2NN testing. Statistics data of SIFT and LPSD correct and wrong matches at different thresholds are respectively plotted as a line chart in Fig. 4(a) and (b).

From Fig. 4, we can observe that with the increase of the threshold, correct matches tend to be constant, while

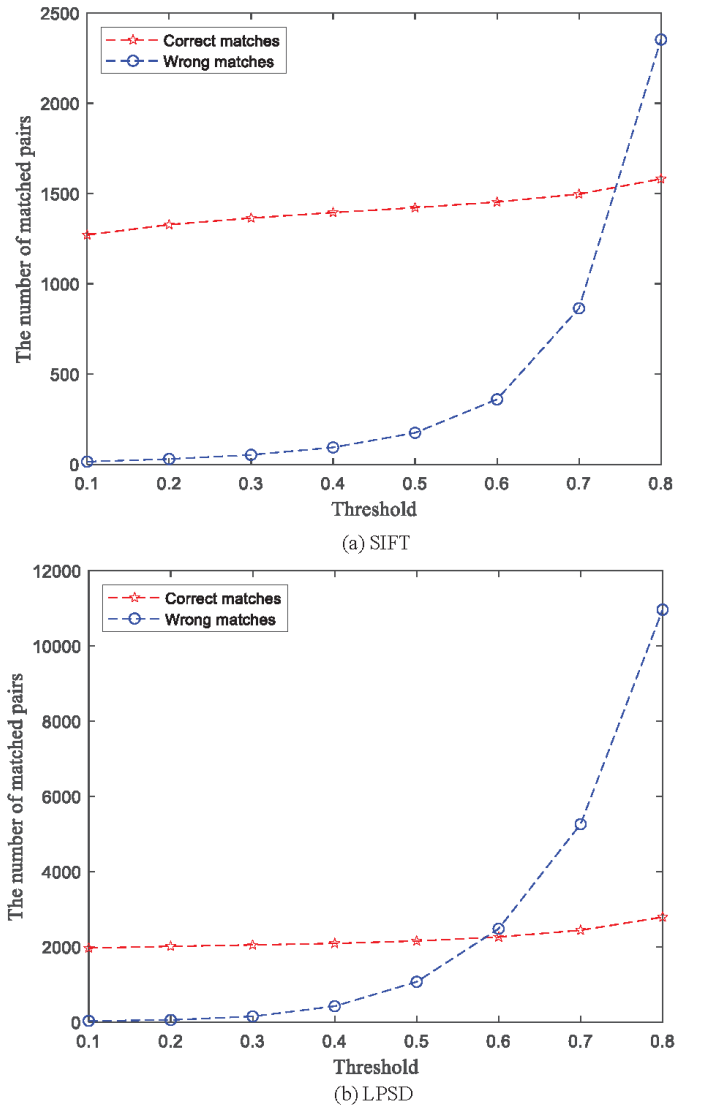


Figure 4. The matching results using different g2NN thresholds with (a) SIFT and (b) LPSD. The correct numbers of matches are depicted in red dashed line with pentagon, while the wrong matches are depicted in dashed line with blue circle.

incorrect matches increase rapidly. Thus, we come to two conclusions:

1) A higher threshold will lead to more false matches, while a lower one may miss some correct matches. It is believed that appropriate threshold should not only obtain as many correct matches as possible, but also guarantee the number of incorrect matches within acceptable limits.

2) Because LPSD has more mismatches at lower thresholds than SIFT descriptor, we set different g2NN thresholds T_{SIFT} and T_{LPSD} for them. The parameters used are presented in Section IV-B.

3.3 Multiple Keypoints Matching

After keypoints matching, we will get a large number of matched pairs. Due to the fact that adjacent keypoints have high similarity, we must remove the matched pairs when

$$\sqrt{(x_a - x_b)^2 + (y_a - y_b)^2} < S, \quad (11)$$

where (x_a, y_a) and (x_b, y_b) indicate the coordinates of matched keypoints.

However, after that, many mismatched pairs still remain, which will seriously put an negative impact on covering or presenting forgery areas. Thus, we employ a widely used and robust algorithm named RANSAC [36] to eliminate them. RANSAC algorithm can estimate a model parameter precisely even when there are lots of mismatched pairs. It divides those pairs into inlier and outlier groups. To get enough matched pairs and, at the same time, to eliminate mismatched pairs with high similarity, our RANSAC algorithm is based on reference [29].

We set the threshold N and loop RANSAC algorithm until the inlier groups points number is less than N . The higher N is, the more mismatched pairs are eliminated. Meanwhile, those slight forgery or low-entropy regions are more likely to be overlooked. By contrast, a lower N is better for detecting those regions. However, it can cause difficulty in eliminating mismatched pairs with high similarity. Therefore, we should get the right balance between the two contradictions.

3.4 Forgery Areas Coverage Algorithm

After postprocessing, we get a number of precise matched pairs; however, these matched pairs can only cover tampered areas partially, which means that the original appearance of those areas cannot be fully revealed. Hence, accurately covering tampered areas is pivotal in CMFD.

In fact, the matching results of block-based methods and keypoint-based methods are essentially the position of two sets of pixels. More specifically, for the coverage of tampered areas, block-based methods require to compare many image block features centered on pixels. If the features of two blocks are sufficiently similar, their central pixels are recorded as a pair of matched points and their corresponding blocks are subsequently covered. Similarly, we consider that keypoint-based methods can also achieve the goal of covering tampered areas by comparing some features, which are within a certain range and centered on pixel points. With the help of keypoint prepositioning, the algorithm complexity can be greatly reduced, thereby improving its detection speed. Thus, we propose a new algorithm to cover tampered areas, which is called ECDC.

3.4.1 Selection of an appropriate feature

Then, for a better coverage, we analyzed and discussed a variety of features. Christlein *et al.* [9] listed most of the effective features, including four types: moment-based, dimensionality reduction-based, intensity-based, and frequency domain-based features. The DCT coefficients of the frequency domain-based features perform well against noise attacks. Wang *et al.* [29], through experiments, concluded that PCET moments perform better than other moment-based features under various geometric transformations. Therefore, we chose DCT coefficients and PCET moments for subsequent experiments.

3.4.2 Block feature matching

We extract block features from two separate circular domains centered on a matched pair. Then, we compare those

features, and if they are similar enough, the corresponding circular domains will be covered. However, different features have different ways to measure their similarity. We usually employ the Euclidean distance to measure the resemblance of PCET moments because its dimension is constant. If the Euclidean distance between $\mathbf{F}_1^{\text{PCET}}$ and $\mathbf{F}_2^{\text{PCET}}$ is smaller than the predefined threshold K_{PCET} , it will be considered as a matched pair, i.e.,

$$\left\| \mathbf{F}_1^{\text{PCET}} - \mathbf{F}_2^{\text{PCET}} \right\|_2 < K_{\text{PCET}}. \quad (12)$$

Concerning the DCT coefficients, the dimension of the matrices depends on the size of sub image blocks. Consequently, large sub image blocks are stored in grand matrices, which is not conducive to computation. Thus, we use singular value decompositions (SVD) [37], [38] to decompose the extracted DCT coefficients matrices, i.e.,

$$\mathbf{F}^{\text{DCT}} = \mathbf{U} \mathbf{\Lambda} \mathbf{V}^T, \quad (13)$$

where \mathbf{U} and \mathbf{V} are unitary matrices and $\mathbf{\Lambda}$ is a diagonal matrix whose entries are the singular values of \mathbf{F}^{DCT} . Since $\mathbf{\Lambda}$ contains the basic information of \mathbf{F}^{DCT} , and its maximum value includes most of the basic information of \mathbf{F}^{DCT} , we choose the maximum value λ of $\mathbf{\Lambda}$ to represent \mathbf{F}^{DCT} of a circular domain, i.e.,

$$\lambda = \max(\mathbf{\Lambda}). \quad (14)$$

If the difference between λ_1 and λ_2 of two circular domains is less than the threshold K_{DCT} , i.e.,

$$|\lambda_1 - \lambda_2| < K_{\text{DCT}}, \quad (15)$$

we determine that these two circular domains are tampered areas. We take 48 images from the benchmark dataset [9], crop their center into sub image blocks of 3×3 , 39×39 , and 75×75 sizes, and attack them in various ways. Then, we calculate the mean value of λ (denoted as $\bar{\lambda}$) in these three sets of sub image blocks, and list the results in Table I. It shows that $\bar{\lambda}$ has only a slight difference under various attacks, which proves the feasibility of representing \mathbf{F}^{DCT} by λ to depict sub image blocks.

Table 1
COMPARISON OF IMAGE BLOCKS $\bar{\lambda}$ UNDER DIFFERENT ATTACKS.

Image Types	$\bar{\lambda}(3 \times 3)$	$\bar{\lambda}(39 \times 39)$	$\bar{\lambda}(75 \times 75)$
Original	328.87	3867.53	7454.32
Rotation(15°)	317.85	3866.56	7434.00
scaling(98%)	328.85	3800.30	7314.76
Noise(0.06)	330.31	3891.77	7496.27

The selection of the aforementioned thresholds K_{PCET} and K_{DCT} has a great influence on the accuracy and robustness of our algorithm. If they decrease, the criteria get more stringent and the coverage is more precise; however, if the image is attacked by noise and geometric transformations, this algorithm would more easily miss or misjudge tampered areas. On the contrary, it is more robust. To make it more robust to noise attacks, we set those thresholds as functions $K_{\text{PCET}}(\sigma_s)$ and $K_{\text{DCT}}(\sigma_s)$, where σ_s is the difference of variance between two circular domains. Finally,

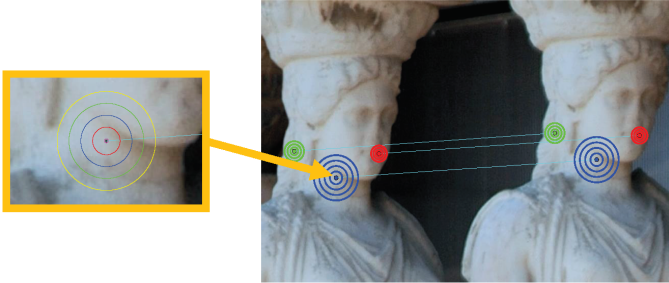


Figure 5. Illustration of the detail of ECDC algorithm. Left: a locally enlarged radii changing process for a keypoint of a match. Right: the radii expansion process of three sets of matched pairs based on ECDC algorithm. Each matched pair is labeled with different colors.

based on numerous experiments, we have established two empirical formulas for $K_{PCET}(\sigma_s)$ and $K_{DCT}(\sigma_s)$, which are piecewise functions:

$$K_{PCET}(\sigma_s) = \begin{cases} 1, & \sigma_s \leq 0.1, \\ 25, & 0.1 < \sigma_s \leq 1, \\ 75, & \sigma_s > 1, \end{cases} \quad (16)$$

$$K_{DCT}(\sigma_s) = \begin{cases} 25, & \sigma_s \leq 1, \\ 50, & 1 < \sigma_s \leq 10, \\ 100, & \sigma_s > 10. \end{cases} \quad (17)$$

3.4.3 Circular domains evolution

Since tampered areas sizes are uncertain, they may not be covered ideally if only the features within a single radius are used as coverage basis. Therefore, we set the radius to an evolving vector in steps of τ :

$$\mathbf{R} = \{r_1, r_2, \dots, r_m\}, \quad (18)$$

where $r_1 < r_2 < \dots < r_m$. In this way, we can compare the features of matched pairs in an evolving radius range by looping.

The detail of ECDC is illustrated in Fig. 5, in which radii changing process for a keypoint of a matched pair is shown in closeup. For ease of interpretation, the rings in the closeup are labeled with different colors. In the first comparison, we compare the features in the red ring centered on one of the matched pair. When the threshold $K \in \{K_{PCET}, K_{DCT}\}$ is met, the radius is enlarged to the size of the blue ring and a second round of comparison is made. If the difference between the features in the blue ring is still less than K , the radius continues to be enlarged until it reaches its maximum or the difference no longer fulfills that condition. Then, the previous radius is recorded and the loop is broken. After traversing all matched pairs with the above algorithm, their coverage is finally completed.

The position of matched pairs is also of great importance on radii expansion. Three expansion results are presented in Fig. 5. The red and green pairs are near the edges of the tampered areas; thus, their rings' extension ends before the radius enlarged to its maximum r_m , which means that ECDC can accurately distinguish the edges. On the contrary, the blue pair is in the center of the tampered areas and, obviously, surrounded by it, so the expansion of the blue ring ends when the radius enlarges to its maximum r_m .

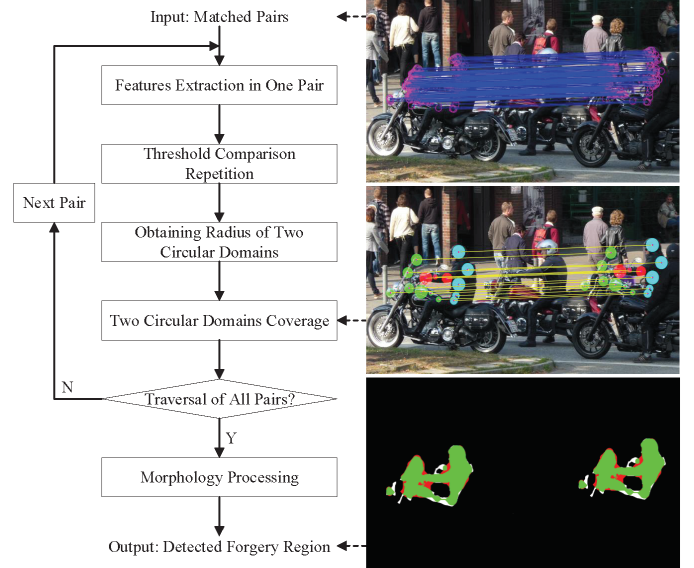


Figure 6. Flowchart of ECDC algorithm.

Fig. 6 presents the flowchart of ECDC algorithm, in which the middle image only partially shows the coverage of matched pairs. Furthermore, Fig. 5 represents the enlarged and detailed diagram of the step 'Threshold Comparison Repetition' of the loop in Fig. 6.

3.4.4 Morphological postprocessing

Finally, depending on the size of the image, the disk size used for close operation varies. This step fills small holes and cracks in the merged areas while maintaining the overall outline of the areas as it is, which is advantageous to completely cover tampered areas.

4 EXPERIMENTAL RESULTS AND ANALYSIS

In this section, we conducted a series of experiments to compare validity and robustness between our scheme and other classic and state-of-the-art schemes. Section IV-A presents the image dataset we used and how we evaluated CMFD schemes. Section IV-B presents our experimental setup, other schemes which we have compared with ours, and our parameters. Section IV-C presents the comparison between the proposed and the mentioned schemes, in terms of their performance in detecting plain copy-move forgery at the image level. Section IV-D presents the comparison between the proposed scheme and other methods, according to their performance in detecting plain copy-move forgery at the pixel level. Sections IV-E and IV-F present the comparison of performance between the proposed and the mentioned schemes based on the dataset. The images in these detection experiments are attacked by various copy-move forgery distortions including rotation, scaling, JPEG compression, and noise addition. Section IV-G presents the comparison of running time. The experiments demonstrate that the proposed scheme achieved a better performance than the other mentioned schemes.

4.1 Choice of Image Dataset and Evaluation Metrics

We chose the aforementioned dataset [9], which is used by many state-of-the-art schemes, to conduct our experiments. This dataset consists of 48 high-resolution uncompressed portable network graphics (PNG) true color images. The average size of these images is 1500×1500 . These images contain both particularly smooth and highly textured areas, with various kinds of forgery regions such as animals, plants, landscapes, cultural relics, etc. Besides, these copy-move forgery regions are attacked by rotation, scaling, downsampling, JPEG compression, and noise addition. The dataset is not just a few meaningless and simple forged images, it provides corresponding ground-truth images which are realistic. Thus, we chose this dataset to objectively evaluate our scheme, and computed the average precision and recall using all these images in this dataset to reduce the randomness of the samples.

At the image level, we focus on the practicality of our scheme to evaluate whether it can distinguish or not the difference between original images and forged images, as our original intention is to expose digital image forgery. However, at the pixel level, we should not only pay attention whether the proposed scheme can distinguish forged images and original images or not, but also present or cover detected forgery regions perfectly. We use two evolution metrics, precision p and recall r [9], [25], [26] to qualitatively and quantitatively evaluate the experiments at the image and pixel levels.

At the image level, the p and r metrics are defined as follows [9]:

$$p = \frac{T_p}{T_p + F_p}, \quad (19)$$

$$r = \frac{T_p}{T_p + F_n}, \quad (20)$$

where T_p is the number of correctly detected forged images, F_p denotes the number of images which have been erroneously detected as forged, and F_n denotes the number of forged images which have not been detected.

At the pixel level, we still use the same equations (19) and (20) to definite p and r , but T_p is changed to denote the number of correctly detected forged pixels, F_p denotes the number of pixels which has been erroneously detected as forged, and F_n denotes the number of forged pixels which has not been detected. p is used to describe the percentage of correctly detected pixels. A higher value of p means there are less erroneous detections. r describes whether the forgery areas are completely covered or not. A higher value of r means the more complete the coverage of forgery areas is.

An intuitive illustration of the relationship between T_p , F_p , and F_n is shown in Fig. 7. As the way of presenting in references [27], [28] is very clear, we decided to employ the same way: green for correct detected areas, red for incorrect detected areas, and white for ground-truth areas, in which forged areas have not been detected.

Moreover, we combine p with r , and obtain another metric F_1 score [9]:

$$F_1 = 2 \times \frac{p \times r}{p + r}, \quad (21)$$

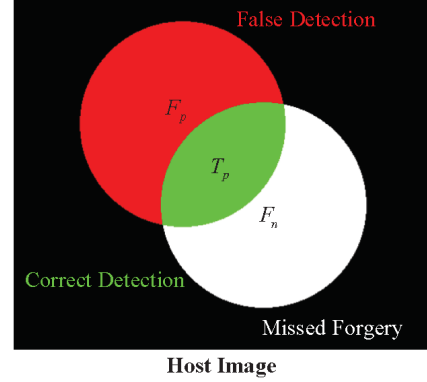


Figure 7. A visualization of the connection between T_p , F_p , and F_n from reference [28].

to evaluate the performances of various CMFD schemes. By using F_1 score, we can directly evaluate these schemes. The higher F_1 score gets, the better the performance is.

4.2 Experimental Setup

The experiments in this paper were performed in MATLAB 2019b on a 64-bit win10 PC with the Intel Core i7-8650 CPU model and 8 GB RAM. As one of our aims is to compare the proposed scheme with some classic and state-of-the-art schemes, we chose, according to Christlein *et al.* [9] experiments, several classic schemes which include both block-based methods (e.g. [14], [15]) and keypoint-based methods (e.g. [20]–[24]). Moreover, we also chose the state-of-the-art schemes (e.g. [18], [25]–[27]) as comparison in our experiments. Finally, we listed the parameters, used in the proposed scheme, in Table II.

Table 2
PARAMETERS SETTING IN THE PROPOSED SCHEME.

Parameters	Values	Meanings
T_{SIFT}	0.6	Threshold of SIFT in g2NN test
T_{LPSD}	0.1	Threshold of LPSD in g2NN test
S	50	Threshold of Euclidean distance
r_1	1.5	Minimum value of radii group
r_m	37.5	Maximum value of radii group
τ	2	Step of radii group

4.3 Detection Results under Plain Copy-Move Forgery at the Image Level

In this section, we mainly examined the ability of each aforementioned scheme to distinguish both original and forged images. The test dataset is based on *orig* and *nul* datasets. The *orig* dataset consists of 48 high-resolution original images without any tampering, while the *nul* dataset contains plain copy-move forgery of the original ones. Of these 96 images, we must correctly distinguish the forged image from the original one. The detection results are listed in Table III, in descending F_1 order. Our scheme achieves the highest level of $p = 97.96\%$, $r = 100\%$, and $F_1 = 98.97\%$ regardless of using DCT or PCET. Of the 48 images from the *orig* dataset, our scheme only mistakenly detects the picture *supermarket* as a forged image, and there is no missing

detection. In summary, the performance of our scheme is better than these classic and state-of-the-art schemes.

Table 3
DETECTION RESULTS UNDER PLAIN COPY-MOVE FORGERY AT THE IMAGE LEVEL IN DESCENDING F_1 ORDER

Schemes	$p(\%)$	$r(\%)$	$F_1(\%)$
ECDC-DCT	97.96	100.00	98.97
ECDC-PCET	97.96	100.00	98.97
Pun [25]	96.00	100.00	97.96
Wang [14]	92.31	100.00	96.00
Ryu [15]	92.31	100.00	96.00
Cozzolino [18]	94.12	97.96	96.00
SURF [21], [23]	91.49	89.58	90.53
Zheng [26]	77.41	94.18	84.98
SIFT [20], [22], [24]	88.37	79.17	83.52
Zandi [27]	63.16	97.96	76.80

4.4 Detection Results under Plain Copy-Move Forgery at the Pixel Level

In this section, we checked the ability of the aforementioned schemes to detect image tampering at the pixel level. We want those schemes to be able to show the forged areas in detail, which means they can perfectly display the particulars in the ideal situation. The detection results of the 48 images from the *nul* dataset are listed in Table IV, in descending F_1 order. The proposed scheme, while using DCT, achieves the optimal F_1 , with $p = 92.61\%$, $r = 91.48\%$, and $p = 91.56\%$. It has better CMFD performance at the pixel level compared with other algorithm. The highest r is achieved when using PCET, because the coverage is more comprehensive; however, this leads to more coverage errors. Wang *et al.* [30] achieved the highest p , which means they had the least number of detection errors. To sum up, our scheme reaches better results at the image level and the pixel level in the case of plain copy-move forgery.

Table 4
DETECTION RESULTS UNDER PLAIN COPY-MOVE FORGERY AT THE PIXEL LEVEL IN DESCENDING F_1 ORDER

Schemes	$p(\%)$	$r(\%)$	$F_1(\%)$
ECDC-DCT	92.61	91.48	91.56
Wang [14]	98.69	85.44	90.92
Ryu [15]	95.07	87.72	90.29
Cozzolino [18]	92.98	88.98	90.19
Pun [25]	97.22	83.73	89.97
Zheng [26]	87.32	85.43	86.27
ECDC-PCET	81.84	93.31	86.09
Zandi [27]	83.65	79.53	79.66
SURF [21], [23]	68.13	76.43	69.54
SIFT [20], [22], [24]	60.80	71.48	63.10

4.5 Detection Results under Various Attacks

As images are not only forged under plain copy-move manipulations, we need to test the robustness of different schemes when they are under various attacks, in order

to comprehensively evaluate those schemes. As a result, forged images are generated using each of the 48 images from the *orig* dataset by attacks of geometric transformations including scaling and rotation, as well as by common signal processing, such as noise, downsampling, and JPEG compression.

4.5.1 Scaling

These experiments were based on three datasets: *scale*, *scaleExtra*, and *scaleExtra2*. In the dataset *scale*, the copy fragments are scaled by scaling factors ranging from 91% to 109% in steps of 2%. In the dataset *scaleExtra* and *scaleExtra2*, the scaling factor is 50%, 80%, 120%, and 200%; therefore, the total number of images is $48 \times 14 = 672$.

4.5.2 Rotation

These experiments were based on three datasets: *rot*, *rotExtra*, and *rotExtra2*. The three datasets rotate the copied fragments by 2° , 4° , 6° , 8° , 10° , 20° , 60° , and 180° ; thus, the total number of detected images is $48 \times 8 = 384$.

4.5.3 Noise

In this part, we conducted two different experiments under noise attacks. It is acknowledged that in many image datasets which are used in CMFD, there are two different ways of adding noise. One, called local noise, consists of adding noise only to the copied fragments as it can be seen in *Inoise* dataset. The other, called global noise, is to add noise to the entire image, which we used on the *nul* dataset. Therefore, our experiments, divided into two groups, add local and global noise respectively, with standard deviations of 0.02–0.1 in steps of 0.02. Each of the two experiments detects $48 \times 5 = 240$ images.

4.5.4 JPEG compression

These experiments were based on *jpeg* dataset. The entire image is under JPEG compression with quality factors between 20–100 in steps of 10. The total number of detected images is $48 \times 9 = 432$.

4.5.5 Downsampling

These experiments were based on *scale-down* dataset. The 48 forged images are downsampled in steps of 20%, from 90% to 10%. The total number of detected images is $48 \times 5 = 240$.

Fig. 8 shows the detection results of our scheme under different attacks. The first and third columns represent forged images. The second and fourth columns are detection results. Fig. 8(a1) and (a3) show the plain copy-move forgery; Fig. 8(b1) and (b3) show the forged fragments scaled respectively by small and large scaling factors; Fig. 8(c1) and (c3) show the images under different rotation angles attacks; Fig. 8(d1) and (d3) show the local noise with two different standard deviations; Fig. 8(e1) and (e3) are the images under global noise attacks with two different standard deviations; Fig. 8(f1) and (f3) show the forged images attacked by JPEG compression with two different quality factors; Fig. 8(g1) and (g3) are two forged images downsampled by different downsampling factors. It can be seen from the results that our scheme also performs well on tampered images or forged fragments under various

geometric transformations and signal processing. In Section IV-F, we plotted the statistics as a line chart to more visibly display the overall performance of the proposed scheme compared with the others.

4.6 Performance Comparison under Various Geometric Transformations and Signal Processing

Figs. 9-11 show the p , r , and F_1 at the pixel level under (a) scaling, (b) rotation, (c) local noise, (d) global noise, (e) JPEG compression, and (f) downsampling attacks with different colors for different schemes' results. Fig. 9 shows the p results of the proposed scheme compared with the aforementioned schemes under different attacks. We can observe that the precision of the proposed scheme surpasses most of the others. Under small-scale rotation and scaling, the proposed scheme performs well, its precision with DCT is higher than that with PCET. In terms of large-scale rotation and scaling attacks, the results of the proposed scheme are superior to most of the others. The test results are displayed in Fig. 8(b2). Remarkably, the precision of our scheme running with DCT reaches more than 80% at large-scale magnification. It also shows the highest results under the most severe global noise attacks. However, our scheme is greatly affected by JPEG compression because of the extraction of many inoperative keypoints, especially when the quality factor is below 30. In this situation, as shown in Fig. 8(f2), our scheme can only maintain good performance to detect large forged areas, as it cannot filter out the invalid matches which are far more than the correct matches, when faced with small tampered areas. Of course, by making parameters of RANSAC and ECDC thresholds more stringent can reduce false coverage and the precision of JPEG compression with a low quality factor can be significantly improved; however, as the number of effective keypoints decreases, the precision of these results will considerably be reduced under local noise and global noise attacks. At this point, after strict filtering and ECDC, there will be only a few remaining matched pairs which do not have the ability to completely cover tampered areas. To sum up, it requires a compromise between performance under serious noise and under JPEG compression with a extremely low quality factor.

From Fig. 10, it also can be observed that the recall of our scheme with PCET is higher than that with DCT; therefore, we recommend using ECDC with PCET in vulnerable situations in order to cover forged areas more completely. Considering Figs. 9 and 10, we note that higher recall leads to lower precision, which means that the larger the coverage is, the lower the accuracy of detection may be. If tampered areas only have to be precisely indicated and they do not need to be presented perfectly, using ECDC with DCT would be a better option because it has higher detection precision with fewer mismatches. It should be mentioned that Tables III and IV show that ECDC with DCT has an excellent detection capability under plain copy-move forgery at not only the image level but also the pixel level.

Fig. 11 depicts the comparison of all F_1 scores. We can intuitively conclude that ECDC is robust against all kinds of attacks whether it is in combination with DCT or PCET. Though the robustness of ECDC against some attacks is slightly inferior to the scheme [18], it is exceptionally better

in large-scale detection compared with most classic and state-of-the-art schemes tested.

4.7 Running Time Comparison

To comprehensively evaluate a CMFD scheme, we should pay attention to its running efficiency in addition to its effectiveness and reliability; thus, we selected 48 images from the *nul* dataset to evaluate the processing efficiency of the proposed scheme and the others. As the experimental platform of Christlein *et al.* [9] is different from ours, we only compare the schemes implemented on the same platform, and record the average running time of each scheme in Table V, in an ascending order. Table V shows that our running time is relatively fast, and it is above average compared with other solutions.

Table 5
DETECTION RESULTS UNDER PLAIN COPY-MOVE FORGERY AT THE PIXEL LEVEL IN DESCENDING F_1 ORDER

Schemes	Running Time (s)
Pun [25]	128.45
Cozzolino [18]	149.03
ECDC-DCT	164.81
Zandi [27]	192.23
ECDC-PCET	275.87
Zheng [26]	554.36

5 CONCLUSION

Nowadays, the phenomenon of easy falsification of images has been a hot spot in the field of digital image forensics and information security. Copy-move forgery is one of the most common manipulations in image forgery. In this paper, we propose a new CMFD scheme based on ECDC. By using the combination of SIFT and LSD extraction algorithms, we get both SIFT and LSD descriptors of the entire image. In this way, those descriptors can get more detail features, while being more robust to various attacks. Then we use g2NN to gain a large number of matched pairs. After that, we use RANSAC to eliminate most of the mismatched pairs and gain more precise matched pairs; thus, forgery regions have been located roughly. Then, to get the accurate forgery regions, we propose ECDC algorithm, which can cover forgery regions according to the block features of evolving circular domains. Finally, we use morphological operations to improve the results of ECDC algorithm.

Nowadays, as the resolution of images gets higher, their size gets larger. Due to the complexity of the matching features step, block-based methods take too much time, and keypoint-based methods have difficulty in perfectly covering forgery regions. These two factors become our driving force to propose this scheme. In that way, we surmount the barriers caused by applying block features or keypoints alone.

We conduct a large number of experiments on the proposed scheme with satisfactory results to testify that it is an advanced scheme in CMFD field. Those results show both high effectiveness and efficiency, a notable increase in



Figure 8. Visualized CMFD results of the proposed scheme under various attacks where (a1), (a3), (b1), (b3), (c1), (c3), (d1), (d3), (f1), (f3), (g1), and (g3) respectively are center park, bricks, christmas hedge, supermarket, ship number, tapestry, sweets, white, lone cat, kore, stone ghost, and jellyfish chaos. The first row shows the forgery images and the detection results under plain copy-move forgery. The second and third rows show the forgery images and the detection results under scaling and rotation. The fourth and fifth rows show the forgery images and the detection results under local noise and global noise, respectively. The sixth and last rows show the forgery images and the detection results under JPEG compression and downampling, respectively. Green is the label of correctly detected regions and false areas are indicated in red. White color specifies the ground-truth areas, in which forged areas have not been detected.

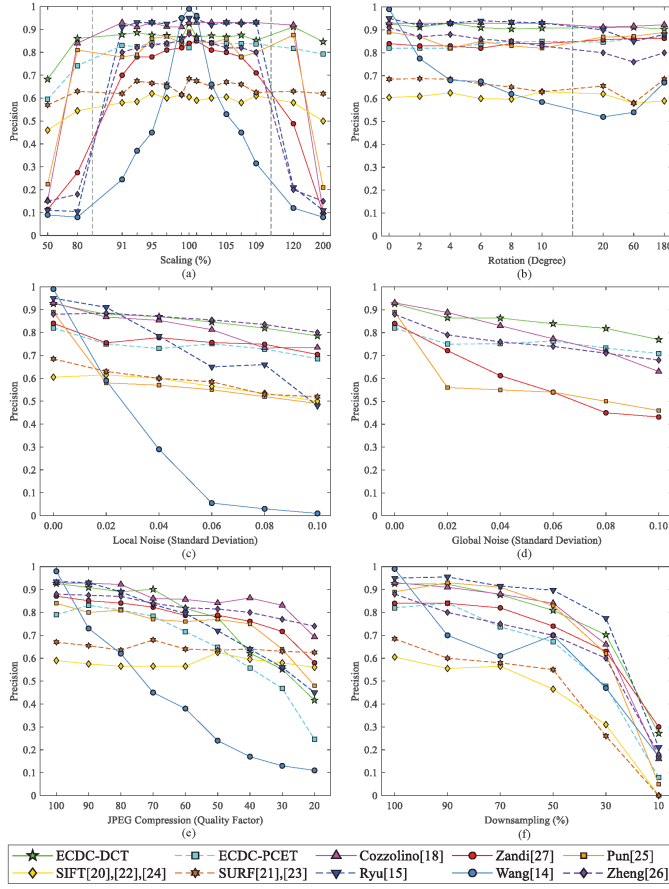


Figure 9. Precision results at the pixel level: (a) Scaling; (b) Rotation; (c) Local noise; (d) Global noise; (e) JPEG compression; (f) Downsampling.

evaluation metrics and running speed. In comparison with other state-of-the-art CMFD schemes, the proposed scheme achieves more outstanding performance, especially under plain copy-move forgery.

In the future, we will strive to combine ECDC with more robust features, and enable it to cope with more various image attacks. Meanwhile, we will research a more flexible and reasonable way of fusing block-based and keypoint-based methods, so that it can get better performance and higher efficiency.

REFERENCES

- [1] S. Sharma and U. Ghanekar, "A rotationally invariant texture descriptor to detect copy move forgery in medical images," in *Proc. IEEE Int. Conf. Comput. Intell. Commun. Technol.*, Ghaziabad, India, 2015, pp. 795–798.
- [2] Photo Tampering Throughout History. Accessed: Nov. 20, 2019. [Online]. Available: https://pth.izitru.com/2016_02_01.html
- [3] C. Wang, H. Zhang, and X. Zhou, "A self-recovery fragile image water-marking with variable watermark capacity," *Appl. Sci.*, vol. 8, no. 4, Apr. 2018, Art. no. 548.
- [4] A. Zear, A. K. Singh, and P. Kumar, "A proposed secure multiple watermarking technique based on DWT, DCT and SVD for application in medicine," *Multimedia Tools Appl.*, vol. 77, no. 4, pp. 4863–4882, Feb. 2018.
- [5] A. Shehab, M. Elhoseny, K. Muhammad, A. K. Sangaiah, P. Yang, H. Huang, and G. Hou, "Secure and robust fragile watermarking scheme for medical images," *IEEE Access*, vol. 6, pp. 10269–10278, Feb. 2018.
- [6] X. Wang, J. Xue, Z. Zheng, Z. Liu, and N. Li, "Image forensic signature for content authenticity analysis," *J. Visual Commun. Image Represent.*, vol. 23, no. 5, pp. 782–797, Jul. 2012.
- [7] M. Okawa, "From BoVW to VLAD with KAZE features: Offline signature verification considering cognitive processes of forensic experts," *Pattern Recogn. Lett.*, vol. 113, pp. 75–82, Oct. 2018.
- [8] M. Okawa, "Synergy of foreground-background images for feature extraction: Offline signature verification using Fisher vector with fused KAZE features," *Pattern Recogn.*, vol. 79, pp. 480–489, Jul. 2018.
- [9] V. Christlein, C. Riess, J. Jordan, C. Riess, and E. Angelopoulou, "An evaluation of popular copy-move forgery detection approaches," *IEEE Trans. Inf. Forensics Secur.*, vol. 7, no. 6, pp. 1841–1854, Dec. 2012.
- [10] J. Fridrich, D. Soukal, and J. Lukáš, "Detection of copy-move forgery in digital images," in *Proc. Digit. Forensic Res. Workshop*, Cleveland, OH, USA, 2003, pp. 55–61.
- [11] A. C. Popescu and H. Farid, "Exposing digital forgeries by detecting duplicated image regions," Dept. Comput. Sci., Dartmouth College, Hanover, NH, USA, Tech. Rep. TR2004-515, 2004.
- [12] S. Bayram, H. T. Sencar, and N. Memon, "An efficient and robust method for detecting copy-move forgery," in *Proc. IEEE Int. Conf. Acoust. Speech Signal Process.*, Taipei, Taiwan, 2009, pp. 1053–1056.
- [13] J. Wang, G. Liu, Z. Zhang, Y. Dai, and Z. Wang, "Fast and robust forensics for image region-duplication forgery," *Acta Auto. Sin.*, vol. 35, no. 12, pp. 1488–1495, Dec. 2009.
- [14] J. Wang, G. Liu, H. Li, Y. Dai, and Z. Wang, "Detection of image region duplication forgery using model with circle block," in *Proc. Int. Conf. Multimedia Inf. Networking Secur.*, Wuhan, China, 2009, pp. 25–29.
- [15] S. Ryu, M. Lee, and H. Lee, "Detection of copy-rotate-move forgery using Zernike moments," in *Proc. Lect. Notes Comput. Sci.*, Alberta, Canada, 2010, pp. 51–56.
- [16] Y. Li, "Image copy-move forgery detection based on polar cosine

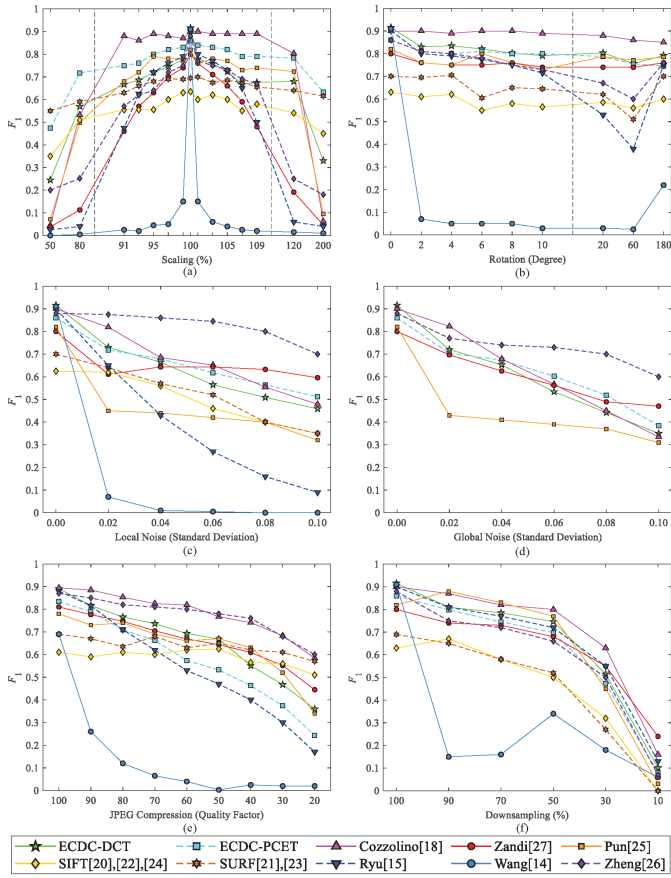


Figure 11. F_1 scores at the pixel level: (a) Scaling; (b) Rotation; (c) Local noise; (d) Global noise; (e) JPEG compression; (f) Downsampling.

transform and approximate nearest neighbor searching," *Forensic Sci. Int.*, vol. 224, no. 1–3, pp. 59–67, Jan. 2013.

[17] P.-T. Yap, X. Jiang, and A. Chichung Kot, "Two-dimensional polar harmonic transforms for invariant image representation," *IEEE Trans. Pattern Anal. Mach. Intell.*, vol. 32, no. 7, pp. 1259–1270, Jul. 2010.

[18] D. Cozzolino, G. Poggi, and L. Verdoliva, "Efficient dense-field copy-move forgery detection," *IEEE Trans. Inf. Forensics Secur.*, vol. 10, no. 11, pp. 2284–2297, Nov. 2015.

[19] D. Cozzolino, G. Poggi, and L. Verdoliva, "Copy-move forgery detection based on PatchMatch," in *Proc. IEEE Int. Conf. Image Process.*, Paris, France, 2014, pp. 5312–5316.

[20] H. Huang, W. Gou, and Y. Zhang, "Detection of copy-move forgery in digital images using SIFT algorithm," in *Proc. Pacific-Asia Workshop Comput. Intel. Ind. Appl.*, Wuhan, China, vol. 2, 2008, pp. 272–276.

[21] B. Xu, J. Wang, G. Liu, and Y. Dai, "Image copy-move forgery detection based on SURF," in *Proc. Int. Conf. Multimedia Inf. Networking Secur.*, Nanjing, China, 2010, pp. 889–892.

[22] I. Amerini, L. Ballan, R. Caldelli, A. Del Bimbo, and G. Serra, "A SIFT-based forensic method for copy-move attack detection and transformation recovery," *IEEE Trans. Inf. Forensics Secur.*, vol. 6, no. 3, pp. 1099–1110, Sept. 2011.

[23] B. L. Shivakumar and S. Baboo, "Detection of region duplication forgery in digital images using SURF," *Int. J. Comput. Sci. Issues*, vol. 8, no. 4–1, pp. 199–205, Jul. 2011.

[24] X. Pan and S. Lyu, "Region duplication detection using image feature matching," *IEEE Trans. Inf. Forensics Secur.*, vol. 5, no. 4, pp. 857–867, Dec. 2010.

[25] C. Pun, X. Yuan, and X. Bi, "Image forgery detection using adaptive oversegmentation and feature point matching," *IEEE Trans. Inf. Forensics Secur.*, vol. 10, no. 8, pp. 1705–1716, Aug. 2015.

[26] J. Zheng, Y. Liu, J. Ren, T. Zhu, Y. Yan, and H. Yang, "Fusion of block and keypoints based approaches for effective copy-move

image forgery detection," *Multidimens. Syst. Signal Proc.*, vol. 27, no. 4, pp. 989–1005, Oct. 2016.

[27] M. Zandi, A. Mahmoudi-Aznaveh, and A. Talebpour, "Iterative copy-move forgery detection based on a new interest point detector," *IEEE Trans. Inf. Forensics Secur.*, vol. 11, no. 11, pp. 2499–2512, Nov. 2016.

[28] C. Pun and J. Chung, "A two-stage localization for copy-move forgery detection," *Inf. Sci.*, vol. 463–464, pp. 33–55, Oct. 2018.

[29] C. Wang, Z. Zhang, Q. Li, and X. Zhou, "An image copy-move forgery detection method based on SURF and PCET," *IEEE Access*, vol. 7, pp. 170032–170047, Dec. 2019.

[30] D. G. Lowe, "Object recognition from local scale-invariant features," in *Proc. IEEE Int. Conf. Comput. Vision*, Kerkyra, Greece, 1999, pp. 1150–1157.

[31] H. Bay, T. Tuytelaars, and L. Van Gool, "SURF: Speeded up robust features," in *Proc. Lect. Notes Comput. Sci.*, Graz, Austria, 2006, pp. 404–417.

[32] W. C. N. Kaura and S. Dhavale, "Analysis of SIFT and SURF features for copy-move image forgery detection," in *Proc. Int. Conf. Innov. Inf., Embed. Commun. Syst.*, Tamil Nadu, India, 2017, pp. 1–4.

[33] R. C. Pandey, S. K. Singh, K. K. Shukla, and R. Agrawal, "Fast and robust passive copy-move forgery detection using SURF and SIFT image features," in *Proc. Int. Conf. Ind. Inf. Syst.*, Gwalior, India, 2014, Art. no. 7036519.

[34] T. Tao and Y. Zhang, "A scale-invariant keypoint detector in log-polar space," in *Proc. SPIE Int. Soc. Opt. Eng.*, Tokyo, Japan, vol. 10225, 2017, Art. no. 102250P.

[35] D. G. Lowe, "Distinctive image features from scale-invariant keypoints," *Int. J. Comput. Vis.*, vol. 60, no. 2, pp. 91–110, Nov. 2004.

[36] M. A. Fischler and R. C. Bolles, "Random sample consensus: A paradigm for model fitting with applications to image analysis and automated cartography," *Commun. ACM*, vol. 24, no. 6, pp. 381–395, Jun. 1981.

[37] G. H. Golub and C. Reinsch, "Singular value decomposition and least squares solutions," *Numer. Math.*, vol. 14, no. 5, pp. 403–420, Apr. 1970.

[38] H. C. Andrews and C. L. Patterson, "Singular value decompositions and digital image processing," *IEEE Trans. Acoust. Speech Signal Process.*, vol. 24, no. 1, pp. 26–53, Feb. 1976.